Chemical Science

Accepted Manuscript

This article can be cited before page numbers have been issued, to do this please use: X. Wang, J. Li, X. Zhu, Z. Xu, S. Xie, S. Chen, Y. Wan, G. Zhang, M. Ge, W. Zhang, C. Wang and R. Li, *Chem. Sci.*, 2026, DOI: 10.1039/D6SC02309F.




ROYAL SOCIETY OF CHEMISTRY

rsc.li/chemical-science

View Article Online
DOI: 10.1039/D6SC02309F

ARTICLE



# Promoting effect of nickel-chromium hydroxide on nickel phosphide nanosheets for efficient hydrogen production coupled with sulfion degradation

Received 00th January 20xx,
Accepted 00th January 20xx

DOI: 10.1039/x0xx00000x

Xiaojun Wang,[a] Jieting Li,[a] Xinyu Zhu,[a] Zehua Xu,[a] Shuixiang Xie,[a] Shutong Chen, Yuxuan Wan,[a] Guangyu Zhang,[a] Mingzheng Ge,[a] Wei Zhang,[a] Chao Wang,*[,b] and Rui-Qing Li*[a]

Electrochemical hydrogen production represents a sustainable approach for hydrogen generation. However, its large-scale practical application is largely limited by the sluggish oxygen evolution reaction (OER). In this study, the thermodynamically favorable sulfion oxidation reaction (SOR) is employed to replace slow OER and nickel phosphide/nickel-chromium hydroxide ($Ni_2P/NiCr(OH)_2$) nanosheets are constructed to achieve low-energy hydrogen production. Benefiting from the interfacial water structure reorganization and electronic structure optimization caused by $NiCr(OH)_2$) introduction, and uniform nanosheet morphology, $Ni_2P/NiCr(OH)_2$ can achieve a current density of 10 mA $cm^{-2}$ at low overpotentials for both hydrogen evolution reaction and SOR. The assembled hybrid water electrolyzer requires small voltages of 0.513 and 0.698 V to reach 10 and 100 mA $cm^{-2}$, significantly lower than those of conventional water electrolysis. Moreover, $Ni_2P/NiCr(OH)_2$ exhibits excellent stability for 800 h at 200 mA $cm^{-2}$ and realizes the conversion of sulfion into valuable elemental sulfur. This work presents a promising strategy for achieving energy-efficient hydrogen generation and resource utilization of sulfide-containing pollutants.

## Introduction

In recent years, the continuous consumption of traditional fossil fuels has caused a series of serious environmental problems.[1] These problems include greenhouse gas emissions and air pollution. They have pushed researchers to speed up the research, development, and industrial application of renewable clean energy and related technologies.[2,3] Hydrogen ($H_2$) has high energy density, pollution-free combustion products, and abundant raw material sources.[4,5] It is recognized as an ideal sustainable energy carrier to replace fossil fuels.[6] Hydrogen plays a pivotal role in alleviating energy demand pressure and constructing a clean energy ecosystem.[7,8] Currently, $H_2$ production pathways include fossil fuel-based $H_2$ production, industrial by-product $H_2$ recovery and water electrolysis.[9,10] Among them, water electrolysis technology with water as raw material exhibits unique advantages and can produce high-purity green hydrogen with near-zero carbon emissions. It is a core hydrogen production technology integrating sustainability and environmental friendliness, and promoting the transformation of energy structure.[11-13]

Water electrolysis typically involves hydrogen evolution reaction (HER) at the cathode to directly produce hydrogen, and oxygen evolution reaction (OER) at the anode with a standard potential as high as 1.23 V *vs.* reversible hydrogen electrode (RHE).[14-16] Therefore, the OER with high theoretical potential and sluggish kinetics results in substantial energy consumption is major bottleneck of overall water splitting (OWS) process. Specifically, actual anodic operating potentials are often significantly higher than 1.23 V due to limited mass transfer resistance, and ohmic polarization in practical electrolysis systems, further exacerbating the energy burden.[17-19] To overcome these limitations, replacing the OER with the oxidation of thermodynamically favorable small molecules has emerged as an attractive strategy.[20-23] This strategy not only effectively reduces the potentials of anodic reactions, but also enables the co-production of value-added chemicals and hydrogen.[24-26] Thereinto, the sulfide oxidation reaction (SOR, $S^{2-} \rightarrow S + 2e^-$) exhibits a lower standard potential of -0.48 V *vs.* RHE compared with the OER. Coupling SOR with HER in the hybrid water electrolyzer (HWE) can significantly reduce energy consumption of $H_2$ production. Furthermore, this strategy can convert sulfur-containing wastewater into valuable elemental sulfur under mild conditions, realizing resource utilization of pollutants, which provides a promising pathway for developing efficient and low-energy-consumption $H_2$ production.[27-29]

Although metal-based electrocatalysts exhibit high catalytic activity for the SOR, the active metal sites are susceptible to corrosion and poisoning by $S^{2-}$ when directly exposed to sulfur-containing electrolytes. This leads to the degradation of catalytic activity and stability. Therefore, developing high activity and durability catalysts is imminent.[30-32] Transition metal phosphides (TMPs) have emerged as a research hotspot due to their advantages of good electrical conductivity, chemical corrosion resistance and

[a] *School of Textile and Clothing, Nantong University, Nantong 226019, PR China. E-mail: liruiqing@ntu.edu.cn*
[b] *School of Chemistry and Chemical Engineering, Yangzhou University, Yangzhou 225002, China; Email: wangchao@yzu.edu.cn*
† Footnotes relating to the title and/or authors should appear here.
Electronic Supplementary Information (ESI) available: [details of any supplementary information available should be included here]. See DOI: 10.1039/x0xx00000x

compositional tunability. Over the past decades, researchers have developed various synthetic methods including hydrothermal method, phosphorization and electrodeposition method, to adjust morphology, electronic structures and reaction energy barriers of TMPs, which display good performances for SOR and HER. For example, Shi *et al.* prepared the Mo-Pt-S composite catalyst *via* electroreduction and pulse electrodeposition methods, which exhibited excellent hydrogen evolution reaction performance with an overpotential of only 30.12 mV at a current density of 10 mA $cm^{-2}$.[33] Yu *et al.* fabricated the FeCoNiCrMn high-entropy alloy (HEA) *via* a two-step process of hydrothermal sulfurization followed by phosphorization. Endowed with abundant lattice defects and lattice strains, the as-prepared HEA exhibits remarkably superior electrocatalytic performance toward SOR.[34] Liang *et al.* successfully synthesized a multiphase NiCoFe-based layered double hydroxide (NiCoFe-LDH) through a facile seed-assisted heterogeneous nucleation strategy. Featuring a unique microscale hydrangea-like morphology, the NiCoFe-LDH boasts an ultra-large specific surface area and synergistic active phases, which collectively provide abundant catalytic interfaces and reactive sites for SOR.[35] Li *et al.* synthesized $Ni_3S_2$/CoNiP material, which shows excellent catalytic performances for HER, SOR, and nitrate reduction reaction ($NO_3RR$).[36] Even though some progress has been made, most exploited catalysts show monofunctional catalytic performances, which can generate the deterioration and incompatibility of catalysts when pairing them in electrolyzer. Therefore, developing bifunctional catalysts for HER and SOR to realize efficient hydrogen production and sulfion upgrading is of utmost urgency.

In this work, the $Ni_2P/NiCr(OH)_2$ nanosheets grown on nickel foam (NF) are successfully prepared *via* hydrothermal and low-temperature calcination methods. The experimental results indicate that the $NiCr(OH)_2$ introduction can reorganize interfacial water structure and optimize electronic structure of $Ni_2P$, which lead to improved catalytic performances of $Ni_2P/NiCr(OH)_2$ for both HER and SOR. The integrated $Ni_2P/NiCr(OH)_2$-based HWE requires a small cell voltage of 0.513 V at 10 mA $cm^{-2}$ and long-term stability for 800 h, which can efficiently upgrade sulfion into valuable sulfur, achieving efficient $H_2$ production and resource utilization of sulfur pollution at low energy consumption.

## Results and discussion

### Synthesis and characterization

The synthesis route of $Ni_2P/NiCr(OH)_2$ is illustrated in Fig. 1a. Two-step hydrothermal reaction is employed to achieve uniform growth of $Ni(OH)_2/NiCr(OH)_2$ precursor on NF, forming nanosheet-like structure. The surface morphology of $Ni(OH)_2$ is characterized using scanning electron microscopy (SEM). As displayed in Fig. 1b and S1a, the $Ni(OH)_2$ product shows a smooth nanosheet structure. In contrast, the $Ni(OH)_2/NiCr(OH)_2$ exhibits hierarchical nanosheet structure after second hydrothermal reaction (Fig. 1c and S1d), where small nanosheets grow on the original $Ni(OH)_2$ nanosheets, implying the increased the specific surface area.[37] Subsequently, target $Ni_2P/NiCr(OH)_2$ precursor is obtained through phosphorization process. SEM images (Fig. 1d and S1c) display that $Ni_2P/NiCr(OH)_2$ preserve similar hierarchical nanosheet structure to precursor without obvious structural alteration. The X-ray diffraction (XRD)

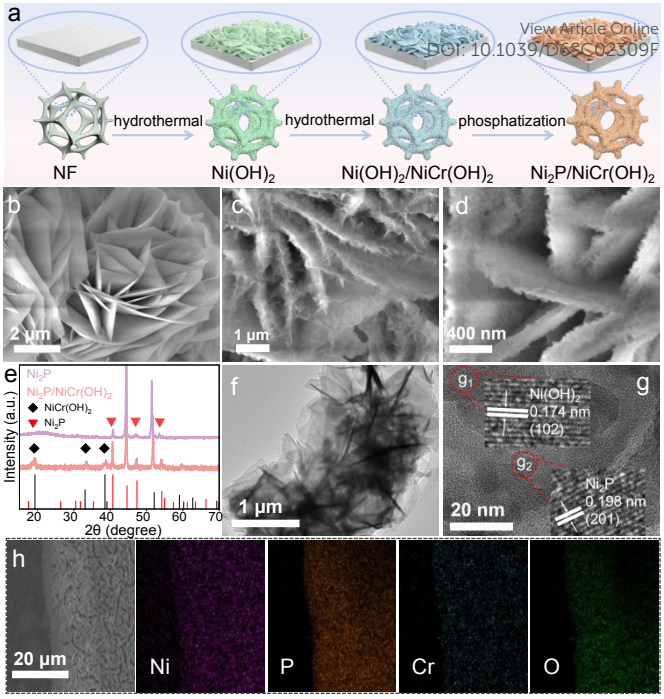


**Fig. 1** (a) Schematic illustration of the synthesis process of $Ni_2P/NiCr(OH)_2$. SEM images of (b) $Ni(OH)_2$ (c) $Ni(OH)_2/NiCr(OH)_2$ and (d) $Ni_2P/NiCr(OH)_2$. (e) XRD patterns, (f) TEM image, (g) HRTEM image and (h) elemental mappings images of $Ni_2P/NiCr(OH)_2$.

patterns of $Ni_2P$ and $Ni_2P/NiCr(OH)_2$ show that characteristic diffraction peaks can be well indexed to $Ni_2P$ (PDF#74-1385) and $Ni(OH)_2$ (PDF#14-0117), confirming the formation of $Ni_2P$ and $Ni_2P/NiCr(OH)_2$ (Fig. 1e). The transmission electron microscopy (TEM) image in Fig. 1f further verifies the layered nanosheet structure. In the high-resolution TEM (HRTEM) image (Fig. 1g), distinct lattice fringes with lattice spacing of 0.174 and 0.198 nm correspond to the (102) plane of $Ni(OH)_2$ and the (201) plane of $Ni_2P$. In Fig. S2, the mass ratio of Ni: P:Cr: O in the $Ni_2P/NiCr(OH)_2$ is calculated to 38.8: 27.0: 3.8: 26.3, which is close to the feeding ratio Ni: Cr. Elemental mapping images of $Ni_2P/NiCr(OH)_2$ (Fig. 1h) confirm the coexistence and homogeneous distribution of Ni, P, Cr and O elements.

X-ray photoelectron spectroscopy (XPS) is employed to further investigate the surface chemical composition and elemental valence states of $Ni_2P$ and $Ni_2P/NiCr(OH)_2$ catalysts. The survey XPS spectrum of $Ni_2P/NiCr(OH)_2$ (Fig. 2a) confirms the coexistence of Ni, P, Cr, and O elements, which is in good agreement with elemental mapping results. While pristine $Ni_2P$ shows characteristic peaks of Ni 2p, P 2p and O 1s, the emerged Cr 2p signal in the $Ni_2P/NiCr(OH)_2$ confirms successful incorporation of Cr. In Fig. 2b, the Ni 2p spectrum of $Ni_2P$ displays two pairs of spin-orbit peaks at 852.4, 856.4 eV, and 872.7, 874.8 eV, belonging to Ni $2p_{3/2}$ and Ni $2p_{1/2}$, respectively. The additional peaks located at 861.6 and 880.2 eV assign to satellite peaks.[38-40] After coupling with $NiCr(OH)_2$, the Ni 2p spectrum of $Ni_2P/NiCr(OH)_2$ reveals a negative shift of 0.7 eV compared with $Ni_2P$, indicating that the electronic structure optimization of $Ni_2P$ and the presence of electronic interaction between $Ni_2P$ and $NiCr(OH)_2$, which are beneficial to improve catalytic performances.[41,42] The P 2p XPS spectrum (Fig. 2c) demonstrates that the characteristic peak at 129.5 eV associates with phosphorus-metal (P-M) bonding configuration, confirming the successful fabrication of $Ni_2P$. The

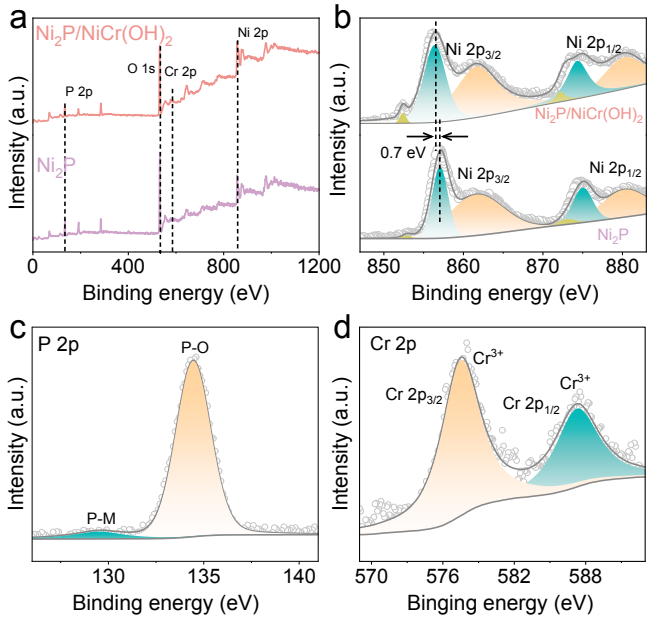


**Fig. 2** (a) XPS spectrum and (b) Ni 2p XPS spectrum of $Ni_2P$ and $Ni_2P/NiCr(OH)_2$. (c) P 2p XPS spectrum and (d) Cr 2p XPS spectrum of $Ni_2P/NiCr(OH)_2$.

broad characteristic peak at 133.8 eV indicates the presence of P-O species on the sample surface, which originates from surface oxidation.[43,44] In high-resolution Cr 2p XPS spectrum (Fig. 2d), two characteristic peaks are observed at binding energies of 587.3 and 577.5 eV, which correspond to the Cr $2p_{1/2}$ and Cr $2p_{3/2}$, respectively. The characteristic peak of Cr $2p_{3/2}$ at 577.5 eV assigns to $Cr^{3+}$, which can modulate the electronic structure and surface active sites, playing a pivotal role in enhancing catalytic performance.[45-47] The O 1s spectra in Fig. S3 reveals the presence of lattice oxygen at 530.9 eV, deficiency oxygen at 531.8 eV, and adsorbed oxygen species at 533.3 eV.[48,49]

**Electrochemical performances**

The electrocatalytic performances of $Ni_2P$ and $Ni_2P/NiCr(OH)_2$ catalysts toward HER are evaluated in a three-electrode system. As shown in Fig. 3a and 3f, the catalytic activities are compared based on linear sweep voltammetry (LSV). The $Ni_2P/NiCr(OH)_2$ requires a low overpotential of 0.111 V to reach a current density of 10 mA $cm^{-2}$, whereas $Ni_2P$ needs high value of 0.230 V, indicating its relatively inferior catalytic activity. The outstanding HER performance of $Ni_2P/NiCr(OH)_2$ outperforms most reported catalysts,as summarized in Fig. 3g and Table S1. When the current density increasing to 300 mA $cm^{-2}$, the required overpotential of $Ni_2P/NiCr(OH)_2$ is as low as 0.281 V, considerably lower than that of $Ni_2P$ (0.456 V) and Pt/C (0.340 V). To further investigate the reaction kinetic, Tafel plots derived from corresponding LSV curves are analyzed. In Fig. 3b and 3f, the Tafel slope of $Ni_2P/NiCr(OH)_2$ is 109.1 mV $dec^{-1}$, lower than that of $Ni_2P$ (162.5 mV $dec^{-1}$), demonstrating that $NiCr(OH)_2$ incorporation can remarkably accelerate catalytic kinetics and achieve high current densities at low overpotentials. The double-layer capacitance values ($C_{dl}$) are calculated from cyclic voltammetry (CV) curves in the non-Faradaic region (Fig. S4) to obtain electrochemical active surface area (ECSA). In Fig. 3c and 3f, the $C_{dl}$ value of $Ni_2P/NiCr(OH)_2$ is 20.6 mF $cm^{-2}$, significantly larger than that of $Ni_2P$ (5.7 mF $cm^{-2}$), suggesting abundant active sites and high intrinsic activity of $Ni_2P/NiCr(OH)_2$. To probe the electrode interfacial properties and charge transfer kinetics, electrochemical impedance spectroscopy (EIS) measurements are conducted. As presented in

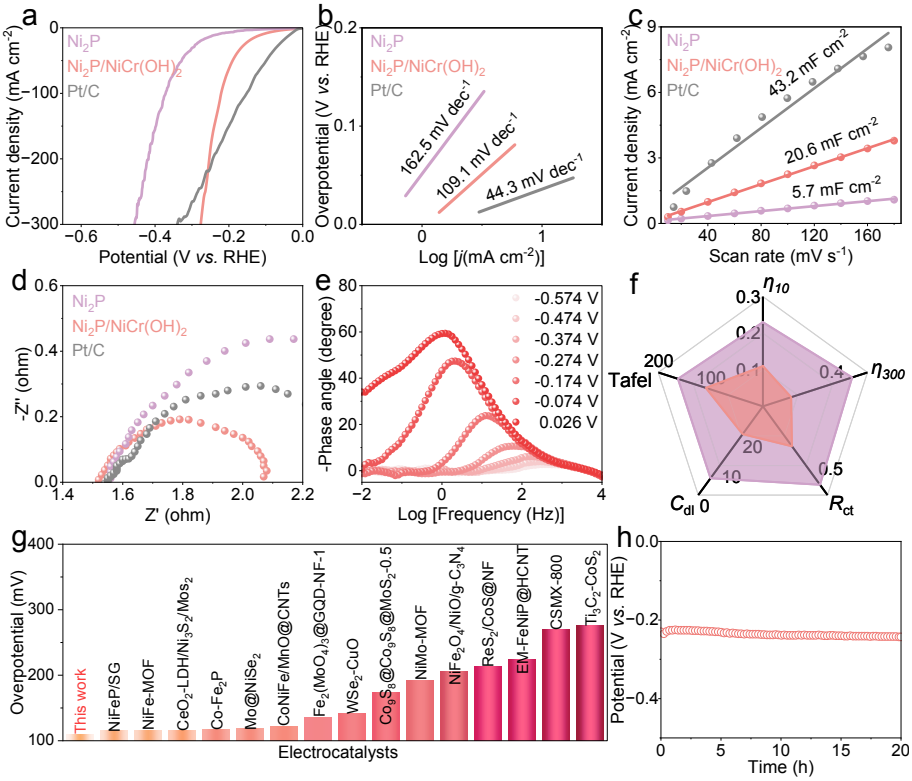


**Fig. 3** (a) Polarization curves, (b) Tafel slope, (c) $C_{dl}$ calculation, (d) EIS plots of different electrocatalysts. (e) Bode phase plots of $Ni_2P/NiCr(OH)_2$. (f) Radar chart and (g) overpotentials comparison. (h) Long-term durability of $Ni_2P/NiCr(OH)_2$.

View Article Online
DOI: 10.1039/D5SC02309F



Fig. 3d and 3f, the charge transfer resistance ($R_{ct}$) of $Ni_2P/NiCr(OH)_2$ is calculated to 0.27 Ω, which is smaller than that of $Ni_2P$ (0.53 Ω), confirming that $NiCr(OH)_2$ introduction is beneficial to reduce charge transfer resistance, accelerate charge transfer and deliver superior electrocatalytic activity. In addition, *in-situ* Bode plots (Fig. 3e and S5) indicate that $Ni_2P/NiCr(OH)_2$ possesses strong capacitive behavior and efficient HER charge transfer kinetics in the high-frequency region. The above results indicate that $NiCr(OH)_2$ introduction plays a crucial role in enhancing HER performances. The long-term stability of catalyst is a key indicator for practical application. In Fig. 3h, the stability test shows that required potentials of $Ni_2P/NiCr(OH)_2$ remain nearly unchanged after continuous operation for 20 h. After the stability, SEM image of $Ni_2P/NiCr(OH)_2$ (Fig. S6) shows that there is no significant change in surface morphology, verifying its excellent structural stability.

The OER performances of $Ni_2P/NiCr(OH)_2$ are further evaluated. As shown in Fig. 4a and 4f, $Ni_2P/NiCr(OH)_2$ exhibites excellent OER activity with small potentials of 1.542 and 1.564 V at 60 and 300 mA $cm^{-2}$, lower than those of $Ni_2P$ (1.563 and 1.608 V) and commercial $RuO_2$ (1.680 and 1.878 V). Moreover, the $C_{dl}$ value of $Ni_2P/NiCr(OH)_2$ (Fig. S7) is higher than that of $Ni_2P$, indicating that $Ni_2P/NiCr(OH)_2$ can expose more catalytic active sites. Considering that the high inherent potentials of OER leads to significant increased energy consumption, the thermodynamically favorable SOR is further explored in 1 M NaOH and 1 M $Na_2S$. In Fig. 4b and 4f, $Ni_2P/NiCr(OH)_2$ displays outstanding SOR activities with small voltages to achieve current densities of 10 and 300 mA $cm^{-2}$ at 0.292 and 0.401 V, obviously lower than those of $Ni_2P$ (0.361 and 0.785 V), indicating that the introduction of $NiCr(OH)_2$ can effectively regulate surface electronic structure of $Ni_2P$ and significantly enhance SOR activity. The required potential for $Ni_2P/NiCr(OH)_2$ is lower than that of other previous developed catalysts (Fig. 4g and Table S2), fully demonstrating its performance advantage in electrocatalytic reactions. To analyze the SOR kinetic advantage of $Ni_2P/NiCr(OH)_2$, the Tafel curves are fitted and systematically analyzed. In Fig. 4c and 4f, the Tafel slope of $Ni_2P/NiCr(OH)_2$ is 24.3 mV $dec^{-1}$, which is much smaller than the of $Ni_2P$ (65.3 mV $dec^{-1}$) and commercial $RuO_2$ (118.2 mV $dec^{-1}$), further implying that $Ni_2P/NiCr(OH)_2$ has a fast SOR kinetic, which can guarantee the efficient progress of SOR. To reveal the intrinsic mechanism of OER and SOR, Bode plots are used to analyze reaction kinetic processes of $Ni_2P$ and $Ni_2P/NiCr(OH)_2$ at different potentials. In Fig. 4d, 4e, and S8, the phase angle of $Ni_2P/NiCr(OH)_2$ is significantly smaller than that of $Ni_2P$ in the low-frequency range, indicating that $Ni_2P/NiCr(OH)_2$ has fast electron transfer rate and reaction kinetic during the OER and SOR. Notably, when the potential increasing to 1.501 V, the phase angles of both $Ni_2P$ and $Ni_2P/NiCr(OH)_2$ decrease sharply, indicating that violent OER occurs, which is in agreement with previous results. In Fig. 4f and S9, the potentials of $Ni_2P/NiCr(OH)_2$ remain nearly stable after continuous operation of 20 h under SOR and OER conditions, respectively. The post-test SEM images (Fig. S10 and S11) reveal that nanosheet morphology of $Ni_2P/NiCr(OH)_2$ are well preserved, demonstrating its outstanding SOR and OER stabilities.

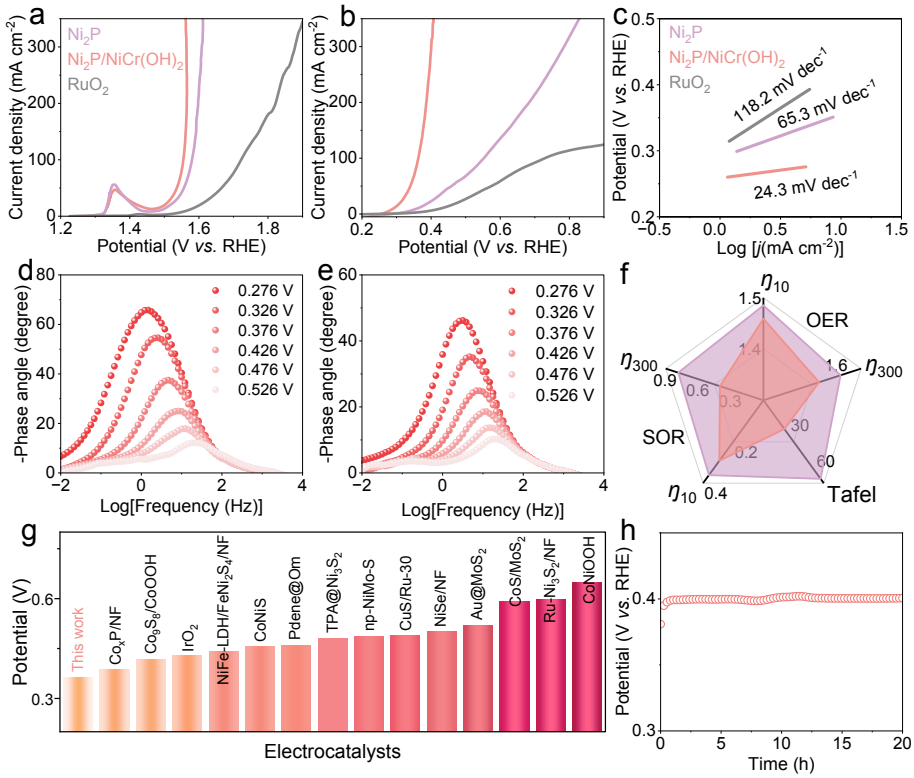


**Fig. 4** (a) LSV curves for OER. (b) LSV curves and (c) Tafel slopes for SOR. (d) Bode phase plots and (e) performances comparison of $Ni_2P$ and $Ni_2P/NiCr(OH)_2$. (g) Overpotentials comparison of developed catalysts and $Ni_2P/NiCr(OH)_2$. (h) Stability measurement for SOR.

View Article Online
DOI: 10.1039/D5SC02309F



Given excellent bifunctional performances of $Ni_2P/NiCr(OH)_2$, the $Ni_2P/NiCr(OH)_2$-based flow electrolyzer (Fig. 5a) is integrated to verify its practical application, which employs a proton exchange membrane to separate cathode and anode chambers, enabling efficient isolation and ions transport of cathodic and anodic reactions. In Fig. 5b, the needed voltages of HWE system are significantly lower than those of HWE systems at the same current density, confirming that replacing the OER with SOR can effectively reduce energy input and achieve energy-saving $H_2$ production. Specifically, the required voltages of HWE are only 0.513 and 0.698 V to attain 10 and 100 $mA{\cdot}cm^{-2}$, much lower than these required in the OWS system (1.647 and 1.876 V) and many previous reported catalysts (Fig. 5d and Table S3). Meanwhile, the $Ni_2P/NiCr(OH)_2$ shows much better electrocatalytic performance than $Ni_2P$, where $NiCr(OH)_2$ effectively boosts charge transfer and optimizes the surface structure. Long-term durability test of $Ni_2P/NiCr(OH)_2$-based electrolyzer is performed. In Fig. 5c, the HWE system driven by $Ni_2P/NiCr(OH)_2$ can ensure stable operation for up to 800 h with negligible voltage variation at 200 mA $cm^{-2}$. Furthermore, post-test SEM image (Fig. S12) reveals that its structure remains largely intact, fully confirming its excellent durability. After the durability test, post-treatment and characterization are performed by adding sulfuric acid into anodic electrolyte to gain yellow powder product, which is verified as elemental sulfur ($S_8$, PDF#77-0145, Fig. S13). The above results indicate that the $Ni_2P/NiCr(OH)_2$-based HWE can achieve efficient conversion of sulfur-containing species into high-value-added elemental sulfur. To further confirm the impact of $NiCr(OH)_2$ introduction on catalytic performances of $Ni_2P$, *in-situ* dark-field optical microscopy (DFLM) technology of $Ni_2P$ and $Ni_2P/NiCr(OH)_2$ is carried out.[50-52] In Fig. 5e and 5f, the $H_2$ bubble begins to generate on the surface of $Ni_2P/NiCr(OH)_2$ at 1 min 29 s, while no gas bubble is observed on the surface of $Ni_2P$. Obvious and intensive gas bubbles occur on $Ni_2P/NiCr(OH)_2$ at 1 min 55 s, whereas the surface of $Ni_2P$ still do not show any phenomenon of gas generation until 2 min 52 s and a large number of $H_2$ bubbles begin to form in $Ni_2P$ at 3 min 20 s. These results directly demonstrate that $Ni_2P/NiCr(OH)_2$ possesses higher catalytic performances and more intense electrochemical reaction process than the $Ni_2P$. Therefore, the $Ni_2P/NiCr(OH)_2$-based HWE by coupling HER and SOR not only effectively reduces overall electrolysis voltages, but also simultaneously realizes the high-value conversion of sulfur-containing wastewater into valuable sulfur product.

The *in-situ* Raman spectroscopy of $Ni_2P$ and $Ni_2P/NiCr(OH)_2$ was performed to analyze catalytic process of HER and SOR processes in 1.0 M NaOH without and with 1.0 M $Na_2S$ electrolyte. For the HER, the interfacial water structures are analyzed (Fig. 6a and 6b), and the broad O-H stretching band (2800-3800 $cm^{-1}$) is deconvolved into three Gaussian peaks located at 3250 $cm^{-1}$, 3420 $cm^{-1}$, and 3590 $cm^{-1}$, which correspond to 4-coordinated H-bond water (4HB-$H_2O$), 2-coordinated H-bond water (2HB-$H_2O$), and the dangling O-H bonds of interfacial water (free-$H_2O$), respectively.[53] As we know, as the hydrogen-bond density among interfacial $H_2O$ molecules increases, corresponding O-H stretching vibration energy reduces, indicating that interfacial $H_2O$ molecules with fewer hydrogen bonds are more easily dissociated. Consequently, the activation energy barrier for interfacial $H_2O$ dissociation follows the order: free-$H_2O$ < 2HB-$H_2O$ < 4HB-$H_2O$. In Fig. 6c and 6d, the $Ni_2P/NiCr(OH)_2$ has a higher proportion of free-$H_2O$ compared with $Ni_2P$, indicating that the

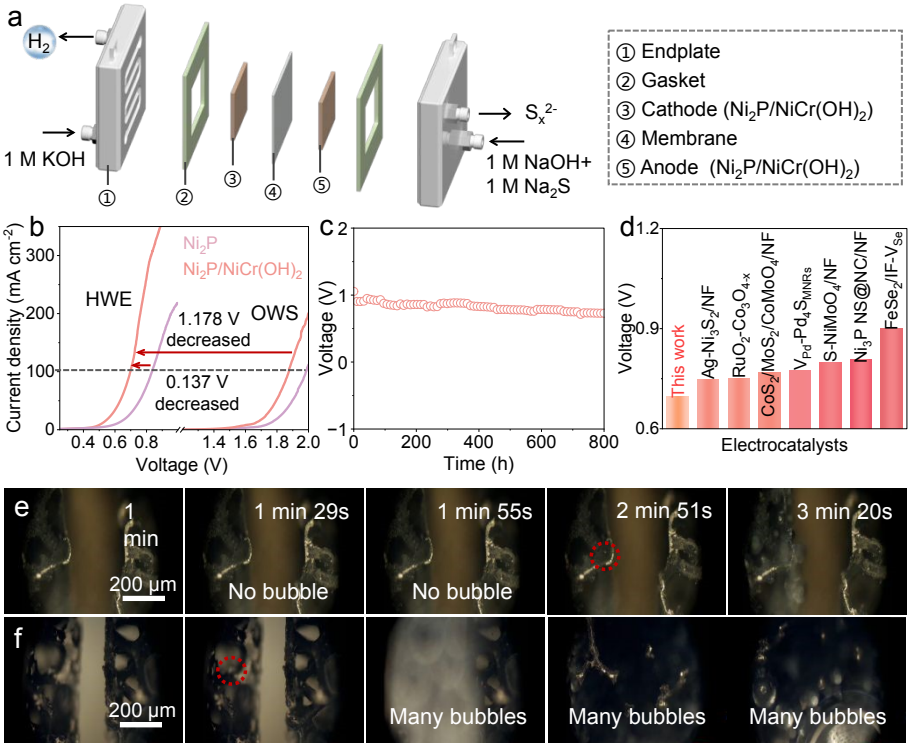


**Fig. 5** (a) Schematic illustration of assembled two-electrode HWE electrolyzer. (b) Polarization curves of HWE and OWS systems. (c) Durability tests of $Ni_2P/NiCr(OH)_2$ for HWE system. (d) Voltages comparison of developed catalysts and $Ni_2P/NiCr(OH)_2$ for HWE systems. The time-lapse DFLM images of (e) $Ni_2P$ and (f) $Ni_2P/NiCr(OH)_2$.

View Article Online
DOI: 10.1039/D6SC02309F



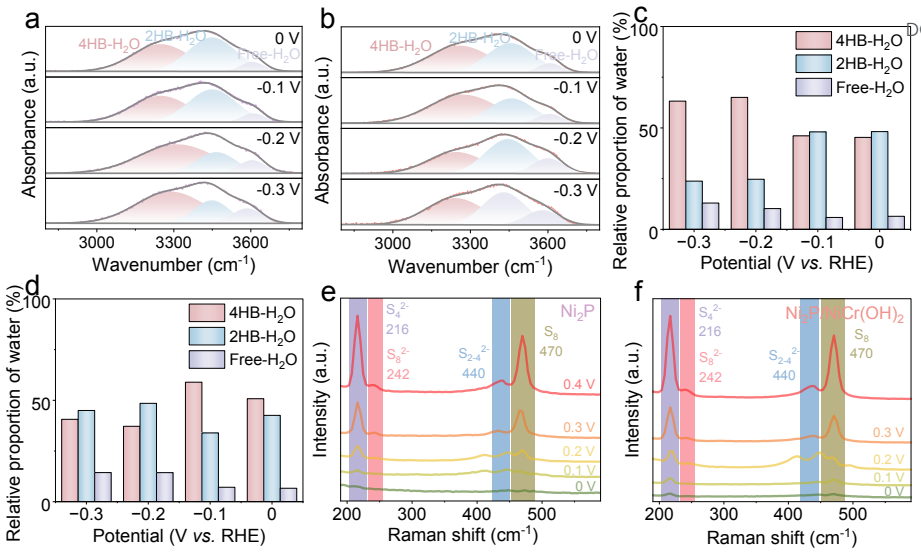


**Fig. 6** Potential -dependent *in situ* ATR-FTIR spectra of the O-H stretching mode of interfacial water on the (a) $Ni_2P$ and (b) $Ni_2P/NiCr(OH)_2$ electrocatalyst surface. The proportions of different types of water for (c) $Ni_2P$ and (d) $Ni_2P/NiCr(OH)_2$. *In-situ* Raman spectra of the electrolytes of (e) $Ni_2P$ and (f) $Ni_2P/NiCr(OH)_2$ at various potentials in 1.0 M NaOH with 1 M $Na_2S$ solution.

enriched free $H_2O$ at the $Ni_2P/NiCr(OH)_2$ interface favors catalytic performance.[54] These results show that the $NiCr(OH)_2$ introduction can restructure interfacial water structure and weaken hydrogen-bond network, which are beneficial $H_2O$ molecule mobility and reorientation, thus accelerating $H_2O$ dissociation to form hydrogen intermediates, thus remarkably enhancing HER activity.[55] For the SOR process, as the potentials gradually increase new characteristic peaks gradually appear at 216, 242, 440 and 470 $cm^{-1}$ on the surface of $Ni_2P$ and $Ni_2P/NiCr(OH)_2$, which belong to $S_4^{2-}$, $S_8^{2-}$, $S_{2-4}^{2-}$ and $S_8$, respectively (Fig. 6e and 6f). These results confirm that a strong SOR responses occurs and the $S^{2-}$ gradually oxidizes to generate the short-chain polysulfur intermediates ($S_x^{2-}$), which eventually form $S_8$ molecules. However, the Raman characteristic peaks of $Ni_2P$ are weaker compared to the $Ni_2P/NiCr(OH)_2$ (Fig. 6e and 6f) with rising potentials, indicating that the introduction of $NiCr(OH)_2$ effectively promotes the conversion of $S^{2-}$ to polysulfide and elemental $S_8$.[56,57] These results verify that the $Ni_2P/NiCr(OH)_2$ has better adsorption and conversion capacities in terms of polysulfide ions than the $Ni_2P$, which effectively facilitates SOR performances.

## Conclusions

In summary, $Ni_2P/NiCr(OH)_2$ nanosheets are successfully fabricated *via* a two-step hydrothermal and phosphorization route. $Ni_2P/NiCr(OH)_2$ exhibits superior bifunctional activities for HER and SOR, which deliver 10 mA $cm^{-2}$ at 111 mV and 292 mV, respectively. *In-situ* Raman and DFLM confirms that $NiCr(OH)_2$ incorporation can reorganize interfacial water structure and boost reaction kinetics. The assembled electrolyzer enables high current densities at low voltages and ultra-long stability for 800 h, obvious lower than those required for traditional water electrolysis. This study provides a strategy to modulate the interfacial water structure and achieve energy-saving hydrogen production and resource utilization of sulfion-rich wastewater.

## Data availability

The relevant experimental and characterization data are available in the article and the ESI.

## Author Contributions

Xiaojun Wang: Data curation and formal analysis. Jieting Li: Investigation. Xinyu Zhu: Formal analysis. Zehua Xu: Investigation. Shuixiang Xie: Data curation. Shutong Chen: Formal analysis. Yuxuan Wan: Data curation. Guangyu Zhang: Investigation. Mingzheng Ge: Investigation. Wei Zhang: Investigation. Chao Wang: Conceptualization & Investigation. Rui-Qing Li: Conceptualization, writing-review & editing.

## Conflicts of interest

There are no conflicts to declare.

## Acknowledgements

This research was supported by the National Natural Science Foundation of China (No. 22302103), the Natural Science Foundation of Jiangsu Province (No. BK20230619), the Natural Science Foundation of the Jiangsu Higher Education Institutions of China (No. 23KJB540003), the Postgraduate Research & Practice Innovation Program of Jiangsu Province (No. KYCX25_3762), the National-Level Innovative Training Program Project for College Students of Nantong University (No. 202510304048), and Nantong University Analysis & Testing Center for SEM characterization.

## Notes and references

1 K. Modi, P. Pataniya, S. Siraj, P. Sahatiya, V. Patel, C. Sumesh, *J. Energy Storage*, 2023, **63**, 107040.
2 R. Li, X. Xu, J. Zeng, X. Zhang, X. Wan, S. Guo, X. Wang, S. Xie, Z. Cao, Y. Zhang, C. Wang, J. Deng, O. Fontaine, M. Ge, J. Dai, G. Zhang, W. Zhang, X. Wang, Y. Zhu, *Nano Lett.*, 2025, **25**, 1272.
3 J. Masnica, S. Sibt-e-Hassan, S. Potgieter-Vermaak, Y. Regmi, L. King, L. Tosheva, *Green Carbon*, 2023, **1**, 160.
4 X. Zhang, Y. Chen, Z. Ye, H. Hu, L. Lei, F. You, J. Yao, H. Yang, X. Jiang, *Chin. J. Struct. Chem.*, 2024, **43**, 100200.
5 S. Chauhan, K. Joshi, P. Pataniya, C. Sumesh, *Sustain. Energy Fuels*, 2025, **9**, 3550.
6 J. Liu, Y. Liu, B. Nan, D. Wang, C. Allen, Z. Gong, G. He, K. Fu, G. Ye, H. Fei, *Angew. Chem., Int. Ed.*, 2025, **64**, e202425196.
7 W. Song, J. Wu, J. Li, Z. Wang, T. He, W. Chen, D. Sun, J. Wu, *Green Carbon*, 2024, **2**, 393.
8 S. Xie, X. Zhu, Y. Zhang, F. Zhang, W. Fan, Z. Yang, G. Zhang, M. Ge, W. Zhang, R. Li, *Chem. Commun.*, 2026, **62**, 1641.
9 Y. Cheng, Y. wang, Z. Shi, H. Wu, J. Yang, J. Ni, M. Yang, Z. Wang, M. Xiao, C. Liu, W. Xing, *EcoEnergy*, 2025, **3**, 131.
10 J. Liang, Z. Cai, X. He, Y. Luo, D. Zheng, S. Sun, Q. Liu, L. Li, W. Chu, S. Alfaifi, F. Luo, Y. Yao, B. Tang, X. Sun, *Chem*, 2024, **10**, 3067.
11 M. Song, X. Yang, C. Guo, S. Zhang, J. Ma, H. Gao, *EcoEnergy*, 2025, **3**, 470.
12 S. Dristy, M. Habib, M. Joni, M. Najibullah, R. Mandavkar, S. Lin, J. Lee, *Chin. J. Struct. Chem.*, 2025, **44**, 100747.
13 C. Wang, L. Zhu, X. Wang, M. Wu, *Green Carbon*, 2025, **3**, 225.
14 H. Tüysüz, *Acc. Chem. Res.*, 2024, **57**, 558.
15 Y. Chen, Y. Liu, L. Li, T. Sakthive, Z. Guo, Z. Dai, *Adv. Funct. Mater.*, 2024, **34**, 2406587.
16 S. Wang, Z. Geng, S. Bi, Y. Wang, Z. Gao, L. Jin, C. Zhang, *Green Energy Environ.*, 2024, **9**, 659.
17 Y. Wang, L. Chen, H. Zhang, M. Humayun, J. Duan, X. Xu, Y. Fu, M. Bououdina, C. Wang, *Green Chem.*, 2023, **25**, 8181.
18 H. Sun, W. Zhang, J. Li, Z. Li, X. Ao, K. Xue, K. Ostrikov, J. Tang, C. Wang, *Appl. Catal., B*, 2021, **284**, 119740.
19 R. L, X. Wang, S. Xie, S. Guo, Z. Cao, Z. Yan, W. Zhang, X. Wan, *Chem. Sci.*, 2025, **16**, 809.
20 X. Zhang, J. Wang, K. Zong, Z. Chen, X. Yang, L. Yang, X. Wang, Z. Chen, *Carbon Energy*, 2025, **7**, e679.
21 Y. Zhang, L. Liao, H. Zhou, Y. Qi, J. Sun, Y. Zhang, Q. Zhou, Y. Wang, D. Tang, F. Yu, *Energy Environ. Sci.*, 2025, **18**, 7695.
22 Y. Ramli, V. Chaerusani, Z. Yang, *Green Carbon*, 2025, **3**, 113.
23 Y. Zhang, H. Wang, J. Lee, Q. Zhang, *Chin. J. Catal.*, 2023, **55**, 44.
24 H. Thakkar, K. Modi, K. Joshi, G. Bhadu, S. Siraj, P. Sahatiya, P. Pataniya, C. Sumesh, *ACS Sustainable Chem. Eng.*, 2024, **12**, 8340.
25 R. Li, X. Wang, S. Xie, S. Guo, Z. Cao, Z. Yan, W. Zhang, X. Wan, *Chem. Sci.*, 2025, **16**, 809.
26 Y. Nie, X. Liu, J. Li, R. Wang, B. Dong, *Chem. Commun.*, 2026, **62**, 594.
27 L. Ai, Y. Tian, T. Xiao, J. Zhang, C. Zhang, J. Jiang, *J. Colloid Interf. Sci.*, 2024, **673**, 607.
28 J. Huo, L. Jin, C. Chen, D. Chen, Z. Xu, C. Wilfred, Q. Xu, J. Lu, *ACS Appl. Materials. Interfaces,* 2023, **15**, 43976.
29 S. Xie, X. Wang, Y. Li, S. Liu, J. Qian, Y. Zhang, L. Jiang, Z. Cao, Z. Yan, X. Wan, Z. Yang, L. Zou, W. Zhang, R. Li, *Chem. Sci.*, 2025, **16**, 12587.
30 C. Duan, C. Tang, S. Yu, L. Li, J. Li, Y. Zhou, *Appl. Catal., B*, 2023, **324**, 122255.
31 H. Yang, X. Long, F. Liu, J. Zhou, N. Chen, R. Feng, Y. Zhang, X. Fu, J. Luo, B. Zhao, *Appl. Catal. B*, 2025, **366**, 125037.
32 X. Li, W. Yu, Y. Wang, R. Liu, Q. Yu, R. Hu, X. Jiang, Q. Gao, H. Liu, J. Yu, W. Zhou, *Chin. Chem. Lett.*, 2024, **35**, 109166.
33 S Shi, M Li, J Zeng, J Wang, G Zeng, Q Zhong, *J. Electroanal. Chem.*, 2025, **986**, 119076.
34 Z. Yu, D. Boukhvalov, H. Tan, D. Xiong, C. Feng, J. Wang, W. Wang, Y. Zhao, K. Xu, W. Su, X. Xiang, F. Lin, H. Huang, F. Zhang, L. Zhang, L. Meng, L. Liu, *Chem. Eng. J.*, 2024, **494**, 153094.
35 Z. Liang, Y. Nian, H. Du, P. Li, M. Wang, G. Ma, *Mater.*, 2025, **18**, 3377.
36 H. Li, J. Ding, Z. Wei, L. Zhuo, I. Shakir, J. Deng, G. Hu, X. Liu, I*nt. J. Hydrogen Energy*, 2026, **199**, 152878.
37 M. Koudahi, L. Naji, *Electrochim. Acta*, 2022, **434**, 141314.
38 M. Yang, J. Ding, Z. Wang, J. Zhang, Z. Peng, X. Liu, *Chin. Chem. Lett.*, 2025, **36**, 110861.
39 S. Liu, Y. Gu, J. Kang, J. Zhang, S. Liu, H. Yang, X. Zhu, M. Ming, *Int. J. Hydrogen Energy*, 2026, **198**, 152670.
40 S. Zhang, X Yang, L. Ma, J. Ma, H. Gao, *Mater. Today Chem.*, 2025, **49**, 103095.
41 L. Wu, L. Yu, F. Zhang, B. McElhenny, D. Luo, A. Karim, S. Chen, Z. Ren. *Adv. Funct. Mater.*, 2021, **31**, 2006484.
42 H. Huo, H. Hou, Y. Yu, J. Xu, W. Chen, S. Wang, D. Min. *Electrochim. Acta*, 2025, **544**, 147697.
43 Z. Wang, G. Yang, P. Tian, X. Li, K. Deng, H. Yu, Y. Xu, H. Wang, L. Wang, *Chem. Eng. J.*, 2023, **473**, 145147.
44 J. Park, H. Yoon, D. Lee, S. Ji, W. Yang, S. Tilley, M. Sung, I. Park, J. Tan, H. Lee, J. Kim, D. Kim, J. Moon, *Appl. Catal., B*, 2022, **305**, 121045.
45 Y. Pei, D. Li, C. Qiu, L. Yan, Z. Li, Z. Yu, W. Fang, Y. Lu, B. Zhang, *Angew. Chem. Int. Ed.*, 2024, **136**, e202411977.
46 Y. Nie, H. Feng, H. Wang, Y. Hu, L. Cao, B. Dong, *Chem. Eng. J.*, 2025, **523**, 168370.
47 F. Sun, Y. Wang, H. Gao, X. Tian, R. Zhu, Y. Zheng, J. Zang, L. Dong, *Appl. Catal. B: Environ.*, 2025, **383**, 126109.
48 R. Li, S. Guo, X. Wang, X. Wan, S. Xie, Y. Liu,C. Wang, G. Zhang, J. Cao, J. Dai, M. Ge, W. Zhang, *Chem. Sci.*, 2024, **15**, 10084.
49 Y. Dang, P. Düngen, J. Hao, X. Sun, Y. Ding, S. Heumann, *Green Carbon*, 2026, 10.1016/j.greenca.2025.10.009.
50 C. Wang, Q. Xie, G. Wang, Y. Lyu, Q. Wang, X. Ma, H. Wang, T. Guo, Y. Wu, J. Han, *Nano Lett.*, 2024, **24**, 13796.
51 C. Wang, H. Wang, X. Ma, T. Guo, A. Zheng, Y. Zhao, X. Li, Y. Wu, S. Li, J. Han, *Nano Lett.*, 2025, **25**, 6556.
52 N. Liu, G. Zhou, A. Yang, X. Yu, F. Shi, J. Sun, J. Zhang, B. Liu, C. Wu, X. Tao, Y. Sun, Y. Cui, S. Chu, *Proc. Natl. Acad. Sci.*, 2019, **116**, 765.
53 Z. Huang, Z. Chen, C. Xu, L. Wang, M. Gao, S. Zhang, T. Isimjan, X. Shi, Y. Ye, L. Chen, J. Wang, X. Yang, Y. Zhu, B. Wu, *Adv. Funct. Mater.*, 2026, e14861.
54 Y. Wan, Y. Tang, Y. Zuo, K. Sun, Z. Zhuang, Y. Zheng, W. Yan, J. Zhang, R. Lv, *Energy Environ. Sci.*, 2025, 18, 7460.
55 J. Zhu, X. Sun, N. Feng, B. Zhao, M. Qiu, J. Xu, W Luo, *J. Am. Chem. Soc.*, 2025, **147**, 47454.

View Article Online
DOI: 10.1039/D6SC02309F

56 Y. Nie, H. Feng, H. Wang, Y. Hu, L. Cao, B. Dong, *Chem. Eng. J.*, 2025, **523**, 168370.
57 C. Duan, C. Tang, S. Yu, L. Li, J. Li, Y. Zhou, *Appl. Catal., B*, 2023, **324**, 122255.



View Article Online
DOI: 10.1039/D6SC02309F

## Data Availability Statement

All relevant data are within the manuscript and its Supplementary Information files.